Continuous Status Monitoring of Industrial Valve Using OCC-Enabled Wireless Sensor Network

Md. Faisal Ahmed, *Graduate Student Member, IEEE*, Moh Khalid Hasan, *Graduate Student Member, IEEE*, Mostafa Zaman Chowdhury, *Senior Member, IEEE*, Nguyen Cong Hoan, and Yeong Min Jang, *Member, IEEE*

***Abstract*— This technical article proposes an instrumentation valve (IV) status monitoring system based on optical camera communication (OCC). A transmitter circuit equipped with a temperature sensor is integrated into each IV. Each transmitter also includes two light-emitting diodes (LEDs) forming an LED group, where one of the LEDs is used to transmit the data. During the reception process, each LED group is recognized and classified using a neural network. Then, the LEDs are individually identified using the region-of-interest detection mechanism. A close circuit television (CCTV) camera is employed to receive the data, which are henceforth stored in a cloud server for further monitoring. An angle measurement algorithm capable of determining the angle generated due to unwanted failure related to the proper closing or opening of the IV is proposed. Additionally, a neural blind deconvolution algorithm is proposed to alleviate the blur effect in the received images. In short, the data transmitted by the LED contain information including valve ID, temperature, and the amount of inflection produced by the IV. The entire OCC system is implemented, and its performance is evaluated using Python 3.7. Data with blurry images are successfully received up to a communication distance of 10 m, whereas the lowest bit error rate (BER) is achieved at a communication distance of 2 m.**

***Index Terms*— Camera-on–off keying (COOK), image processing, neural network (NN), optical camera communication (OCC), rolling shutter effect.**

I. Introduction

DURING the last decade, instrumentation valves (IVs) have been commonly used in the gas industry. These IVs are often operated by signals, programmed to have a set point for a predetermined process variable. Generally, an industrial gas plant may contain hundreds of IVs, whose status monitoring is an enormously challenging task [1]. Moreover, gas leakage can be immensely toxic and hazardous to the health of the workers [2]. Hence, it is essential to design an efficient IV status-monitoring system to control the gas spread during leakages to escape possible upheavals. It is also imperative to reduce direct human interaction resulting from proneness to distraction, while the gas factory environments can also be noxious [3].

Wireless sensor networks have recently provided a new dimension to next-generation Internet-of-things systems [4]. They have been successfully deployed in numerous applications, such as home or industrial automation, smart structures, and health monitoring. Wireless sensing devices can be integrated with IVs to transmit important information to remote monitors, including valve ID, temperature, and humidity [5]. Radio frequency (RF)-based devices are currently used for IV monitoring. However, massive interference can be generated considering the huge number of IVs in a single factory room, significantly reducing the communication system's performance [6]. Moreover, continuous exposure to RF energy can cause serious long-term effects on the health of workers [7]. Bluetooth is the most-commonly used technology because of its good energy efficiency and low-power consumption [8]. Nevertheless, recent studies have shown that Bluetooth exhibits low radio transmission efficiency because it does not provide any asynchronous channels between the master and the slave [9]. In this article, an optical camera communication (OCC) scheme is recommended to replace RF for data transmission. OCC [10] is a subset of optical wireless communications (OWCs) [11], and it is implemented using light-emitting diodes (LEDs) as the transmitter and a camera as the receiver. Advantages, such as immunity to electromagnetic interference, high security, and low cost, make OCC an immensely potential and reliable technology for next-generation OWC systems [12].

Herein, a factory environment is assumed to contain hundreds of IVs, where each IV comprises sensing and transmitter sections. The sensing section may contain humidity- and temperature-sensing circuits. It is worth mentioning that we have implemented an AM2302 [13] sensor to collect temperature information only. In this article, the IVs considered have a 180° rotating system capable of changing its status from ON to OFF or vice versa. A couple of LEDs are used in the transmitter section, where one is modulated with information collected

Manuscript received September 18, 2021; revised October 28, 2021; accepted November 10, 2021. Date of publication November 23, 2021; date of current version March 2, 2022. This work was supported by the Ministry of Science and Information and Communication Technology (ICT) (MSIT), South Korea, through the Information Technology Research Center (ITRC) support program supervised by the Institute for Information & Communications Technology Planning & Evaluation (IITP) under Grant IITP-2021-0-01396. The Associate Editor coordinating the review process was Dr. Shutao Li. *(Corresponding author: Yeong Min Jang.)*

Md. Faisal Ahmed, Nguyen Cong Hoan, and Yeong Min Jang are with the Department of Electronics Engineering, Kookmin University, Seoul 02707, South Korea (e-mail: faisal.ahmed@ieee.org; conghoan.tdhbka@gmail.com; yjang@kookmin.ac.kr).

Moh Khalid Hasan is with the Department of Electrical and Computer Engineering, Stevens Institute of Technology, Hoboken, NJ 07030 USA (e-mail: mhasan12@stevens.edu).

Mostafa Zaman Chowdhury is with the Department of Electrical and Electronic Engineering, Khulna University of Engineering & Technology, Khulna 9203, Bangladesh (e-mail: mzceee@ieee.org).

Digital Object Identifier 10.1109/TIM.2021.3130292

from the sensor. In particular, the data contain the ID of each IV, ON/OFF status, and temperature. Camera-on–off keying (COOK), a scheme standardized in IEEE 802.15.7-2018 [14], is used to modulate the LED, as this type of modulation has the advantage of providing a higher amount of data per rolling shutter image. A close circuit television (CCTV) camera is used to receive the data sent from the LED. Afterward, the data are stored in a CSV file and subsequently sent to a cloud server for further analysis. Due to the very small size of the LED, we have developed a neural network (NN) capable of precisely detecting and recognizing the region of interest (RoI). Furthermore, unwanted gas leakage may transpire if the IV is not completely ON/OFF as expected. There is an angle misalignment resulting from the different orientations of the transmitter section projected on the image sensor. An algorithm, based on the total number of occupied pixels, can estimate this angle and is also presented in this article. In case of an emergency, the leaked gas can create a smoky environment, and the received image becomes blurry. The smoky environment is simulated to generate blurry images, and a neural blind deconvolution [15] algorithm is proposed to reconstruct the stripes generated due to the camera's rolling shutter effect.

In [16] and [17], the authors have implemented the RoI-based LED detection techniques considering the OCC systems reported in the literature. However, most of these techniques cannot distinguish between data transmitting and interfering LEDs with similar properties. The NN-based RoI detection technique presented in this article is capable of precisely classify and recognize a data transmitting LED in an LED group integrated with IVs. In [18], a system to detect the RoI based on an NN was implemented. Yet, the authors could only demonstrate their work at communication distance of 50 cm. Furthermore, NN-based RoI detection techniques were proposed in [19]–[21], but they exhibited poor bit error rate (BER) performance. Additionally, the NN-based vehicular LED group detection was reported in [22], which only the focused on detection at high-mobility conditions without considering the data received from the LED. The image sensor experiences the blur effect in OCC systems due to the channel characteristics and out-of-focus problem [23]. Consequently, the stripes in the images overlap and can be deformed when the blur intensity is high. Although some image-processing techniques capable of reconstructing a blurry image have been proposed in the literature [24], [25], no research on OCC systems has been conducted to alleviate the blur effect and reconstruct the stripe pattern. In summary, the main contributions of the article are listed as follows.

1) An OCC-based IV status-monitoring system is proposed where two LEDs integrated with an IV operate as a transmitter group, and a low-speed CCTV camera is used as the receiver. The rolling shutter effect of the camera is used to decode the information transmitted from the LEDs. In the proposed system, temperature data are continuously collected from an AM2302 sensor as the information is transmitted using COOK modulation with one LED, and the camera receives data concurrently.
2) An NN model is proposed to efficiently detect and classify each LED group, considering the position variation of the LEDs during the change in the IV status.
3) An algorithm is developed to estimate the amount of inflection affecting each LED group during a gas leakage, and the IV status is continuously updated accordingly.
4) A method based on a neural blind deconvolution algorithm is proposed and implemented to eliminate the blur effect in the images caused by a fumy channel. Additionally, a denoising method is employed to remove the noise coming from adjacent light sources. The entire system is implemented, and its performance is analyzed using Python 3.7.

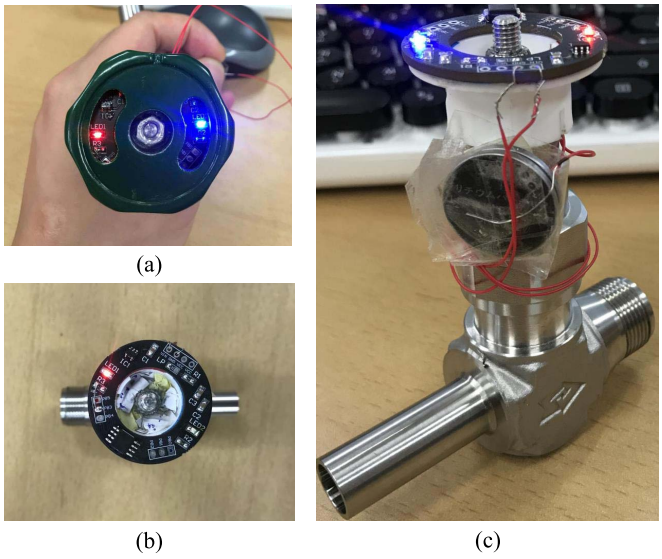

Fig. 1. (a) IV front view with LEDs, (b) complete transmitter section, and (c) complete overview of the IV with the integrated transmitter.

The rest of the article is organized as follows. First, the IV overview and data acquisition from the transmitter circuit are presented in Section II. Next, the proposed OCC system architecture is described in Section III. Section IV presents the stripe pattern reconstruction process from the blurry image. Then, the angle measurement and status-monitoring strategy are presented in Section V, and the data decoding process is described in Section VI. The performance evaluation and a discussion of the research findings are provided in Section VII. Finally, Section VIII concludes the article.

II. Overview and Data Acquisition

In this study, a V81 series Ball valve was considered to implement the suggested monitoring scheme [26]. The IV is used in numerous onshore and offshore applications, especially in gas industries. Fig. 1 illustrates the overall IV architecture where Fig. 1(a) shows the top view of the IV with the lid on, Fig. 1(b) depicts the LED transmitter circuitry, and

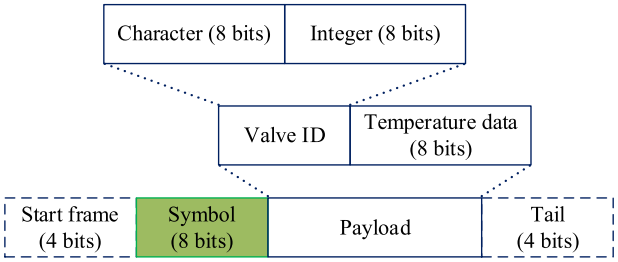

Fig. 2. Data frame structure of the transmitted signal.

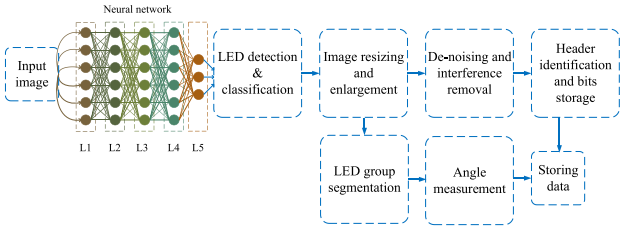

Fig. 3. Receiver data decoding and display procedure.

Fig. 1(c) demonstrates the entire IV architecture combined with the transmitter. Moreover, an AM2302 sensor [13] is integrated with the transmitter to collect the temperature data. An ATMEL 1430 TINY85 20SU microcontroller [27] operated in C language is used to process the sensor data and modulate the LED. The sensor data are mainly composed of integer and decimal values. Five different datasets are considered, for each data packet, where each set contains eight bits of binary data. The first two datasets represent the integer, and the other two datasets are decimal data values. The sum of the first four datasets must be equal to the fifth set, otherwise, the collected data are considered erroneous. The fifth set (named as "checksum") contains eight bits of binary data. Finally, the integer and decimal values are integrated to generate 16-b binary data. Then, these data are converted to decimal values and divided by 10 to generate the final temperature data.

III. Proposed OCC Architecture

A substantial number of IVs may exist in a factory environment; two IVs are implemented in this study for simplicity. Each IV contains a transmitter comprising two LEDs (which form an LED group) with each of them of 3-mm diameter. One LED is used to transmit the temperature data, and the other is used to calculate the fault and inflection. The data related to the temperature and valve ID are composed of character, integer, and symbol. The length of the binary bit sequence regarding those data are different; therefore, each type of data is converted into 1-B binary sequence. However, as a result the possibility of long string of logic LOW or logic HIGH becomes high; therefore, Manchester coding technique is used. As shown in Fig. 2, each frame comprises five parts, i.e., the start frame, symbol, ID, temperature data, and tail. The start frame and tail signify the start and end of each data frame represented as 1011 and 1110, respectively. In addition, the symbol is assigned after the header to avoid errors due to similar bit sequences, which may appear in the ID and temperature data. The valve ID consists of a character and an integer (8-b binary value after conversion). Then, the entire bit-stream is encoded using Manchester coding. Afterward, the data are modulated using COOK, which is an IEEE 802.15.7-2018-standardized scheme. In this work, the blinking frequency of the LED is kept fixed at 2 kHz. A CCTV camera is employed to receive the data. Initially, the LEDs are detected using an NN, which is trained using around 1000 images to generate the weight values. After detecting the LEDs and applying necessary cropping mechanism, a zooming technique is applied based on super resolution technique. Afterward, the blurry images are reconstructed using the proposed neural blind deconvolution algorithm. Subsequently, the stripe patterns are processed, and the data are demodulated. Concurrently, the proposed algorithm to measure the fault and inflection is applied and the information of the IV status is collected. Next, the IV status and ID is separated from the temperature data and stored as a CSV file in the system. The data are simultaneously stored in a cloud server for monitoring. The data reception mechanism is further explained in Sections IV and VII.

IV. Data Reception Process

A CCTV camera (C7837WIP PnP IPCAM) [28], supporting 30 frames per second, is employed to receive the valve ID and temperature data. The camera image sensor receives the optical signal transmitted from each LED group and generates and processes the images frame-wise in real-time utilizing Python, as shown in Fig. 3. Before processing an image, the exposure time is adjusted to remove background illumination and recognize the stripe patterns. It is also initialized with a specific focus value. The LED group is detected using an NN-based technique performed in the Python environment. The main advantage of using the proposed NN is that it is capable of classifying numerous image datasets and recognizing the LED object in the images that have the same features as the trained images. The Python environment is used for training the images by considering different LED shapes generated in the image sensor due to varying different communication distances.

The proposed NN mainly comprises of three key parts: convolutional layer, pooling layer, and fully connected layer. We have used leaky ReLU as the activation function as it can reduce the slope of the mapping function considering the use of a large number of negative values. The operation of the activation function is performed using the rectified correlations on a sphere model. The input image is first processed with necessary padding and striding operations in the convolutional and pooling layers, leading to the output image denoted as z_l, which is converted to a 1-D vector to use as the input of the fully connected layer. Afterward, the output of the kth node of the jth layer is presented as

$$a_k^{[j]} = \sum_{l=1}^{n_{j-1}} w_{k,l}^{[j]} z_l^{[j-1]} \tag{1}$$

where $w_{k,l}^{[j]}$ and $z_l^{[j-1]}$ are represented as the weight and input neurons, respectively. After applying the activation function, the output at the jth layer is expressed as

$$z_k^{[j]} = \max\left(0.1a_k^{[j]}, a_k^{[j]}\right) = LRec\left(a_k^{[j]}\right). \tag{2}$$

Next, we have added a bias to the output vector a_k, which is considered as a constant vector estimated as $\mu = (\sum_{l=1}^{n_{j-1}} z_l^{[j]}/n_{j-1})$. After applying the bias, the output vector is finally updated as follows:

$$z_{k_{\text{update}}}^{[j]} = LRec\left(a_k^{[j]} + \mu w_{k,0}^{[j]}\right); \quad w_{k,0}^{[j]} = -\sum_{l=1}^{N} w_{k,l}^{[j]}$$
$$= LRec\left(a_{k_{\text{update}}}^{[j]}\right). \tag{3}$$

The loss is calculated from the target output and the final output of the network. Then, backpropagation is performed to update the weight using 2000 epochs and a 0.01 learning rate. The final weight is used for the testing purposes. In the testing image frame, the detection mechanism is applied by generating a bounding box containing the LED group, and the coordinate information of each box edge is stored.

Notably that each image frame contains two LED groups in the recommended implementation. A computer program has been developed to crop and separate the regions of each LED group. Then, each cropped image is processed simultaneously in a few steps. First, the image is converted into the grayscale format, where each pixel represents a specific intensity value ranging from 0 to 255. Subsequently, the image is converted to a binary format using a threshold. A smoothing technique is used to enhance the image structure during image processing. Then, the image is processed using dilation and erosion by employing a kernel 7×7 matrix concentration. These steps are used to achieve a clear view of the stripe pattern for data decoding.

The data are decoded using the COOK demodulation technique, where the bright and dark stripe patterns are analyzed. A binary bit stream is generated using a certain threshold. The binary pattern starts saving its value after detecting the start frame and ends when the tail is found. The saved binary format contains the valve ID and temperature information, which are decoded based on the ASCII values. The temperature data and individual valve ID are displayed in the Python environment and are saved in separate CSV files. If the ID is missing or the bending angle has exceeded the threshold, the system sends a warning to the server.

V. Stripe Pattern Reformation

Blurry images may appear for several reasons, such as IV movement, camera misfocus, dirty lens, camera internal vibration, and unstable focal length. Additionally, the communication channel can be affected by the smoke in the factory environment. The optical signal propagating through this fumy channel may produce a blurry image in the image sensor. The blur effect mainly occurs when the changes in the screen are faster than the bandwidth of the camera. Generally, a blurred image can be presented as follows:

$$B = K \bigotimes X + n \tag{4}$$

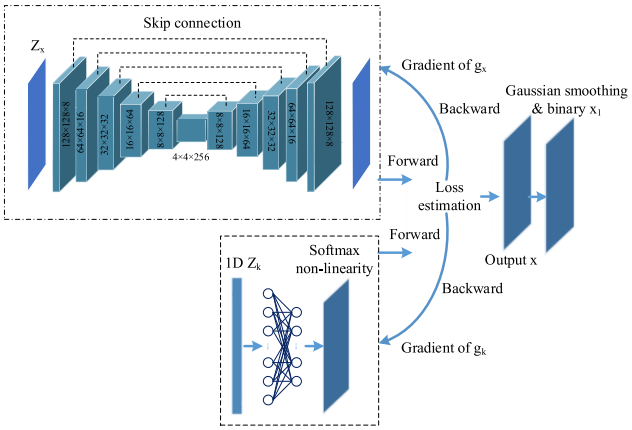

Fig. 4. Blurry image processing using the neural blind deconvolution algorithm.

where X, K, and n are the input image, blur kernel, and unwanted noise from the surrounding environment, respectively. The neural blind deconvolution algorithm, a zero-shot self-supervised learning approach, is suggested to process a blurry image for reconstructing the original stripe pattern. The main objective of the algorithm is to reconstruct the sharp stripe pattern. The deconvolution process follows three principal steps: processing using deep image priors, updating the kernel using a fully connected network, and final image processing through denoising and Gaussian smoothing. The overall deconvolution process is illustrated in Fig. 4.

The deep image prior is a generative network, denoted as g_x. The uniform distribution of each element of the blurred image X is used as an input. The generative model g_x is composed of an autoencoder (used in the input layer) and a sigmoid nonlinearity function (used in the output layer). The autoencoder consists of five encoder and decoder sublayers, linked using a skip connection. On the other hand, the fully connected layer is also a generative network, represented as g_k. It uses a 1-D noise vector with K elements as input and a $K \times K$ matrix as output, called the blur kernel. The output layer of g_k uses a softmax nonlinearity function to satisfy the nonnegative and equality constraints. Both generative networks update their properties based on backpropagation. We have used two generative networks of input images and blur kernels. Therefore, the prior corresponding to those generative models will be $-\log(\Pr(B|g_k, g_x)) = ||g_k \bigotimes g_x - B||^2$. Now, to estimate the posterior, two regularization terms $-\log(\Pr(g_k)) = \alpha(g_k)$ and $-\log(\Pr(g_x)) = \beta(g_x)$ are defined. Based on (1), we can calculate the maximum posterior of the blind convolution algorithm as follows:

$$(g_x, g_k) = \min_{(g_x, g_k)} \left|\left| g_k \bigotimes g_x - B \right|\right|^2 + \delta\alpha(g_k) + \zeta\beta(g_x)$$
$$\text{s.t. } 0 \le (g_k)_m \le 1 \quad \forall m$$
$$(g_x)_n \ge 0, \quad \sum_n (g_x)_n = 1 \ \forall n \tag{5}$$

where the trade-off regularization parameters δ and ζ are controlled based on the noise level. In our implementation, we considered $\delta = 0.2\sigma$ and $\zeta = 0.15\sigma$, where σ is

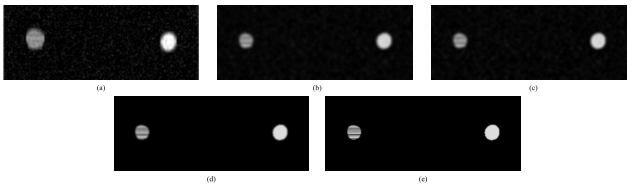

Fig. 5. (a) Input noisy blurry image; output image after (b) 200 iterations and 15 × 15 kernel size, and (c) 200 iterations, and 13 × 13 kernel size; (d) image after applying denoising function, and (e) Gaussian smoothing and binarization of the image.

the noise level. Finally, the generative model g_x is updated using the previous g_x as well as the updated kernel k, and presented as

$$g_{x\text{update}} = \min_{(g_x, g_k)} \left\| g_{k\text{update}} \bigotimes g_x - B \right\|^2 + \zeta\beta(g_x). \quad (6)$$

After completing the iterations, the original image is reconstructed from the final values of g_x. The noise in the output image is subsequently eliminated after applying the regularization parameter, ensuring the robustness of the deconvolution performance. However, the resulting image still contains low-level noise, which is then removed using a fast image denoising function. Finally, the image with the sharp stripe pattern is obtained using Gaussian smoothing and binarization. The step-by-step procedure for obtaining the deblurred image is presented in Algorithm 1. Some results after applying the proposed algorithm are shown in Fig. 5. using different kernel sizes.

Algorithm 1 Image Processing Using Neural Blind Deconvolution

Input: Blur image **y**

Output: Image with sharp stripe pattern **x**, $k \times k$ kernel matrix

Initialization: z_x, z_k (uniform distribution of image and noise kernel), and i

1: **while** $i <= iteration$ **do**
2: increment i
3: $k = g_k^{i-1}(z_k)$
4: $x = g_x^{i-1}(z_x)$
5: run backpropagation for g_x and g_k
6: update g_x and g_k
7: **end while**
8: set $x = g_x^{iteration}(z_x)$ and $k = g_k^{iteration}(z_k)$
9: update with fast image denoising function
10: update with Gaussian smoothing and binarize

VI. Angle Measurement and Status Updating

During the altering state period, a IV may experience a fault. This fault implies that the IV is not completely open or closed. Before proceeding to the details, the reference state of a specific LED group needs to be clarified. The reference state refers to the LED positions of an LED group where the transmitters are projected in the image sensor parallel to the vertical or horizontal axis. In the case of an IV fault, a certain angle (represented as ζ_l) with respect to the reference position is created. Considering the reference state, ζ_l is the same in the projected image. For the remaining cases, an angle with respect to the reference position in the projected image may be created even though the IV is in its usual open or close position. This angle is denoted as ζ_b, and the positions are termed as inflected states. Notably, ζ_b should be taken into account when estimating ζ_l.

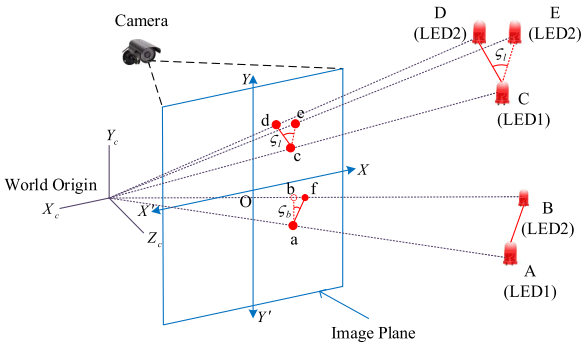

Fig. 6. LED image formation procedure in the projected image coordinates.

In recapitulation, three different scenarios (namely, an inflected state, a fault, while the LED group is in the reference state, and a fault, while the LED group is in the inflected state) are considered. As shown in Fig. 6, the image sensor is assumed to have a 2-D coordinate system, where the coordinates of each LED in the image sensor refer to its center position. The global coordinates of the LEDs are transformed into camera coordinates and eventually to image sensor coordinates using the translation and rotation matrices with the help of the camera intrinsic parameters.

Fig. 6 presents the projection of the LED group in the image sensor for various positions such as the reference (cd), faulty (ce), and inflected positions (ab). The distance between the LEDs is presented as d_s. The complete process for estimating ζ_l is shown in Algorithm 2. Notably the fault is categorized into two types based on whether the IV is expected to be opened or closed. In a reference position, the abscissas or ordinates of the LEDs after the state change (from open to close or vice versa) should be the same. In the inflected state, the LEDs in a specific group appear in the projected image with varying shapes. In this case, ζ_b is calculated using the number of pixels occupied by each LED. Then, the coordinates of the LEDs are compared with their coordinates in previous frames before the state change. Finally, ζ_l is estimated after the LED position is altered. The projected LED images of the IV's reference state at a communication distance of 8 and 2 m are shown in Fig. 7(a) and (b), respectively. The reference state is exhibited at a communication distance of 5 m with a reflective surface in Fig. 7(c). As shown in Fig. 7(d), the LED images at the reference state are shown with an interference coming from another LED. The valve position with a right-side displacement with $\zeta_b = 5.13$ but no fault is shown in Fig. 7(e). Finally, the LED images with a right-side

Algorithm 2 Angle Measurement and Status Update

Input: x_1, x_2, y_1, y_2
Output: Status, ζ_l
Initialization: Threshold
set diameter of L_1, $L_2 = DL_1$, DL_2
set total number of pixel of L_1, $L_2 = NL_1$, NL_2
if $x_1 = x_2$ or $y_1 = y_2$ **then**
  $\zeta_l = 0$
  call Status()
else
  if $DL_1 = DL_2$ **then**
    estimate ζ_l
    call Status()
  else
    if $NL_1 > NL_2$ **then**
      set $NL_2 = NL_1$
      call Bending(L_2)
    else
      set $NL_1 = NL_2$
      call Bending(L_1)
    end if
  end if
end if
Function Status()
Draw DL_1 parallel to frame vertical axis
if pixel i $= DL_1.count(whereDL_1[i] > Theshold)$ **then**
  v_o true
else
  v_c true
end if
Function Bending()
calculate bending angle ζ_b
if $Qx' = Qx$ **then**
  call Status()
else
  take initial NL_x
  estimate new leakage angle ζ_l'
  $\zeta_l = \zeta_l' - \zeta_b$
  call Status()
end if

displacement with $\zeta_b = 5.13$ and $\zeta_l = 22.95$ are displayed in Fig. 7(f). It is noted that all LED images are presented after performing group detection, blur processing, and necessary zooming. The real-valve photos corresponding to the projected images of Fig. 7(a) and (f) are presented in Fig. 7(g) and (h), respectively. The red LED in the middle indicates whether the transmitter is active or not. The entire flow diagram from image capturing to data decoding is presented in Appendix.

VII. Performance Evaluation

The first step in implementing of the monitoring system is the detection and recognition of each LED group. As a result, two LED groups are used in the experiment. An NN was trained using 1000 images and designed to detect and classify each group and weight values produced. These values were

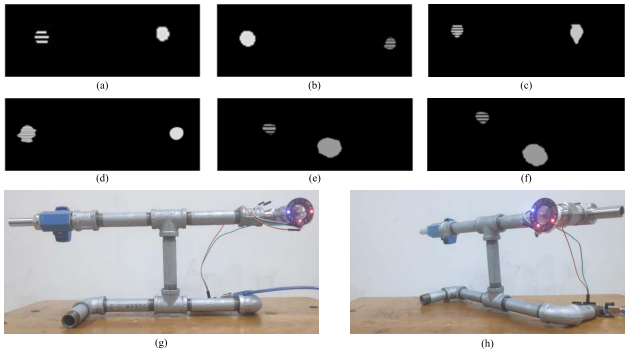

Fig. 7. Reference state at communication distance of (a) 8 m and (b) 2 m; at communication distance of 5 m (c) with a reflective surface and (d) interference (around 1377 lux) generated from another LED; right-side displacement with $\zeta_b = 5.13$, (e) $\zeta_l = 0$, and (f) $\zeta_l = 22.95$; real-valve photos corresponding to the states shown (g) at (a), and (h) at (f) without changing the position of the camera.

subsequently utilized while operating with the test images. Each image is segmented to process each group separately after detection. Then, each LED from the group is identified using RoI detection. Subsequently, each group is binarized, and four types of data (i.e., valve ID and status, temperature, and ζ_l) are extracted. The data are collected based on the normalized intensity of the light source. The entire process of data collection is shown in Fig. 8. Note that, all the angles in this article are presented in degrees.

When the distance between the camera and the LED group increases, the size of the LED reduces rapidly. This problem can be overcome by applying a proper zooming mechanism. However, the distance between the LEDs of a specific group decreases as distance increases. Separating the LEDs is a challenging task once the intensity overlap exceeds a specific limit. Consequently, the distance between the LEDs increases, taking the distance between the IV and camera into account; however, this also increases the size of the transmitter system. Therefore, a minimum distance of 3 cm between the LEDs is set, and the minimum distance required for d_s when the IV-to-camera distance increases is obtained. On the other hand, the estimated value of ζ_l becomes erroneous because of the deformation of the LED shape. The error increases as ζ_l increases; however, it decreases when the distance between the LEDs increases. In general, although OCC performance greatly depends on the communication distance, the increase in error probability with respect to the increasing communication distance is only around 5% as shown in Fig. 9(a)–(c). The main reason is that although the size of the LED changes rapidly with communication distance, our algorithm only considers the center point of the projected image while estimating ζ_l. Conversely, the center of the projected image shifts considerably with ζ_b; as a result, the error in angle measurement is higher than that measured in the case of different ζ_l. However, when the LED size is too small, the variation in the shape of the LED projected image is not significant, consequently leading to an almost constant error probability. On the other hand, with higher d_s, the overlapping possibility of the LED intensities is low, resulting in a lower error probability as shown in Fig. 9(c).

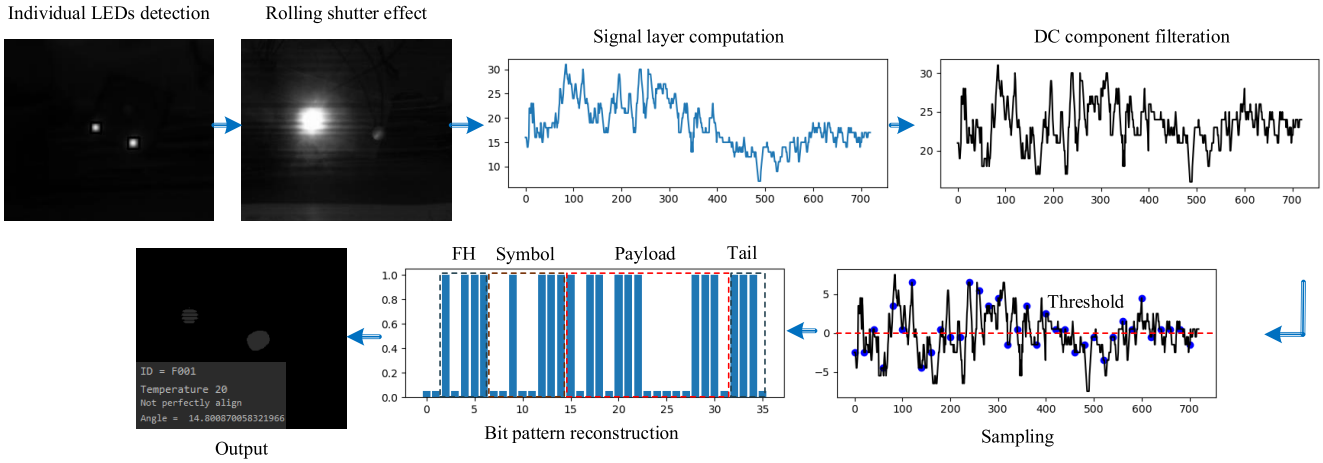

Fig. 8. Entire process of data decoding at the receiver.

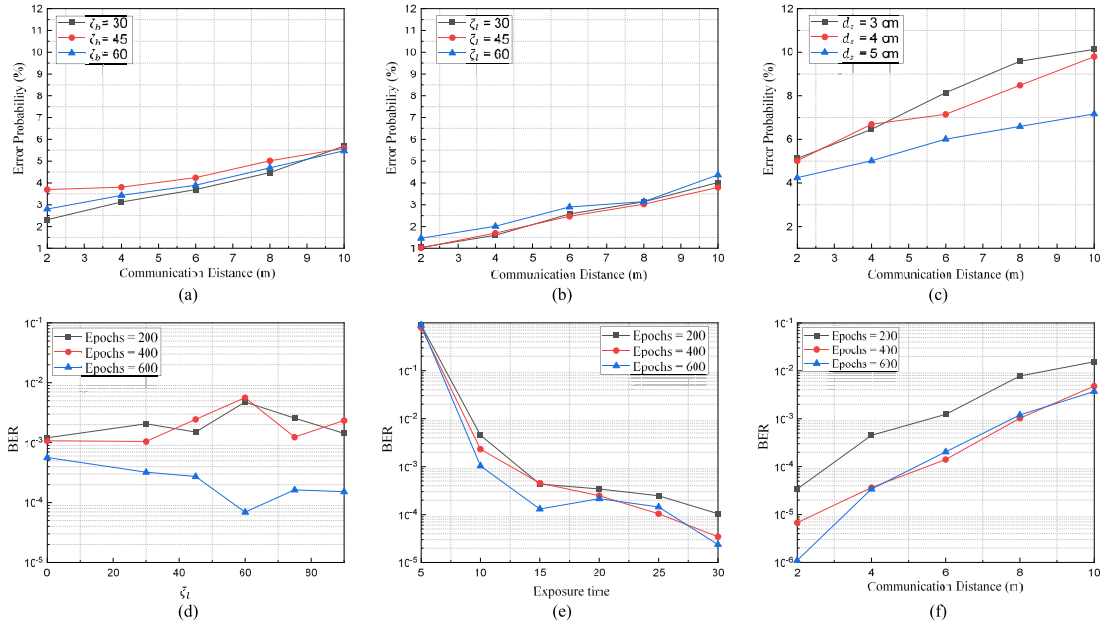

Fig. 9. Angle measurement error for different (a) ζ_l (keeping $\zeta_b = 0$), (b) ζ_b (keeping $\zeta_l = 45$), and (c) d_s (keeping $\zeta_l = 30$ & $\zeta_b = 0$); and BER measurement with respect to (d) ζ_l, (e) exposure time, and (f) communication distance by using the NN at the receiver.

The communication performance is degraded if the image is blurry, as the bright and dark regions in the image overlap. Thus, the neural blind deconvolution algorithm was applied to alleviate the blur effect. The estimated BER for a communication distance of up to 10 m with blurry image frames. It is noted that the blur kernel and output image are produced by running the algorithm for a certain number of epochs. For a higher number of epochs, a more accurate output image can be produced. Therefore, the BER can be significantly improved by increasing the number of epochs shown in Fig. 9(d)–(f). The BER performance is measured by varying ζ_l, exposure time, and communication distance. Unlike the case with ζ_l, it can be seen in Fig. 9(e) that there are noticeable changes in BER with exposure time. The main reason is that the intensity of the bright and dark stripes greatly depends on the exposure time. Here, we presented the exposure time using Python predefined values in the range of 5 (31.3 ms)–30 (0.93 ns). The BER also significantly changes with increasing communication distance. However, the problem can be significantly remediated using the zooming mechanism.

Additionally, the salient edges while processing a blurry image can be recognized using a minimum of 20 epochs. However, the time complexity increases with the number of epochs. This problem can be alleviated using a powerful processor. When applying the COOK demodulation technique on the binarized images, the extracted data of a specific IV are saved in a corresponding CSV file. Information, such as valve ID, status, temperature value, and amount of inflection for each IV, are stored in a cloud server for further analysis. If any unwanted scenario arises, such as link blockage due to a failure in the transmitter circuit or an inflection value higher than the allowed limit, an alarming unit is activated for instant response.

To the best of the authors′ knowledge, this is the first work that propose and implement OCC for the

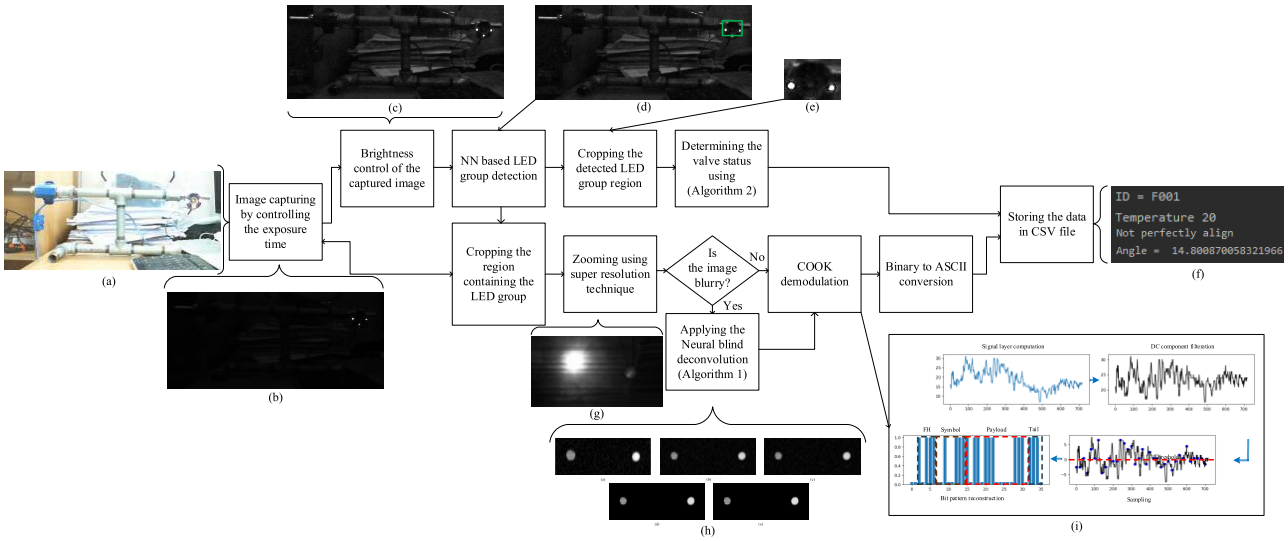

Fig. 10. Complete flow diagram of the proposed IV monitoring system.

TABLE I
PERFORMANCE COMPARISON WITH RELATED OCC SYSTEM

Reference	Method	Distance (m)	Average Error rate
[29]	Bokeh effect	2 m	3.48%
[30]	Adaptive window thresholding	2.1 m	5.3 %
[24]	Blur equalization method based on Wiener filtering	1.5 m	10 %
[31]	Gaussian filter and convolution	30 m	11 %
[32]	Conditional probability	Around 10 m	5 %
This work	Neural blind deconvolution	2 m, 10 m	1.97%, 4.87%

IV monitoring objective. The COOK scheme used in our work is also adopted in another article [16]. Therein, MIMO-COOK was presented, and a data rate of 0.88 kbps was achieved using two data-transmitting LEDs and an LED array. However, although we have used a single LED for data transmission, the achieved data rate is 0.6 kbps when the IV is in the reference state, which can be further augmented to 1.2 kbps if we include another data transmitting LED. On the other hand, different methods were used to reconstruct the stripes in the existing OCC works, but few considered blurry images. Most of the works lacked technical depth and mostly considered simulations based on a single test scenario. In addition, none of them considered NN concept to reconstruct the stripes precisely. Furthermore, we have achieved better performance with the updated blurry images when the IV is in a reference state, as listed in Table I.

VIII. CONCLUSION

In this article, an industrial IV-status-monitoring system based on an OCC system was proposed and implemented in a testbed. The OCC transmitter was composed of an LED group. One of the LEDs in the group was modulated using COOK to transmit the data. The transmitter and AM2302 sensing circuits were integrated into the IV, and the data were transmitted to a CCTV camera. After being collected in a CSV file, the data were stored in a cloud server. An NN-based group detection mechanism was proposed, where each LED was identified using the RoI detection mechanism. An algorithm was developed to measure the inflection angle produced, when the IV was not completely closed or opened as expected. Furthermore, a neural blind deconvolution algorithm was proposed to reconstruct the stripe patterns when the images were blurry. The measured results showed that the data received with the blurry images could be successfully decoded for a communication distance of up to 10 m. Although the BER increases with the communication distance, it can be significantly reduced by increasing the number of epochs in the execution of the proposed algorithm.

APPENDIX
ENTIRE FLOW DIAGRAM OF THE RECEIVER

The complete flow diagram of our developed OCC-based IV status-monitoring system is presented in Fig. 10. The procedures are summarized as follows.

Step 1: The images are captured and processed by controlling the exposure time, resulting in removing the background. The images before and after controlling the exposure time are shown in Fig. 10(a) and (b).

Step 2: A program is developed to increase the intensity of the captured gray-scale image as shown in Fig. 10(c). Afterward, the LED group is detected using the developed NN as shown in Fig. 10(d).

Step 3: Eventually, the LED groups are detected, and necessary cropping mechanisms are applied which is shown in Fig. 10(e). From the cropped images, the program determines the fault and inflection using Algorithm 2. Then, the information is stored in a separate CSV file as illustrated in Fig. 10(f).

Step 4: Meanwhile, after the detected LED group is cropped, a zooming mechanism is executed based on super

resolution technique. Then, that region is focused to capture the rolling shutter effect as shown in Fig. 10(g).

Step 5: Afterward, the presence of blur will be checked. To remove the blur effect, the neural blind deconvolution algorithm is implemented. The algorithm mainly reproduces the deformed stripe pattern created due to the blur as shown in Fig. 10(h).

Step 6: The data are decoded using the COOK demodulation scheme. First, the rolling shutter effect is captured. Then, the normalized intensity is measured from the image before filtering out the dc components of the signal. After applying proper thresholding mechanism, the data are finally decoded using Manchester decoding and stored in the CSV file as shown in Fig. 10(i) and (f), respectively.

REFERENCES

[1] G. Wang, M. Nixon, and M. Boudreaux, "Toward cloud-assisted industrial IoT platform for large-scale continuous condition monitoring," *Proc. IEEE*, vol. 107, no. 6, pp. 1193–1205, Jun. 2019.

[2] *Health and Safety in Valve Operations—Human Factors Engineering (HFE)*. Accessed: Jan. 1, 2021. [Online]. Available: https://www.sofisglobal.com/health-and-safety-in-valve-operations/

[3] *Addressing the Human Factor in Major Accident Risk*. Accessed: Jan. 1, 2021. [Online]. Available: https://www.dnvgl.com/services/human-factors-1094

[4] A. Karaagac, E. De Poorter, and J. Hoebeke, "In-band network telemetry in industrial wireless sensor networks," *IEEE Trans. Netw. Service Manage.*, vol. 17, no. 1, pp. 517–531, Mar. 2020.

[5] N. C. Hoan, N. V. Hoa, V. T. Luan, and Y. M. Jang, "Design and implementation of a monitoring system using optical camera communication for a smart factory," *Appl. Sci.*, vol. 9, no. 23, p. 5103, Nov. 2019.

[6] C. M. Caffrey, T. Sillanpää, H. Huovila, J. Nikunen. S. Hakulinen, and P. Pursula, "Energy autonomous wireless valve leakage monitoring system with acoustic emission sensor," *IEEE Trans. Circuits Syst. I, Reg. Papers*, vol. 64, no. 11, pp. 2884–2893, Nov. 2017.

[7] A. Ahlbom, A. Green, L. Kheifets, D. Savitz, and A. Swerdlow, "Epidemiology of health effects of radiofrequency exposure," *Environ. Med.*, vol. 112, no. 17, pp. 1741–1754, 2004.

[8] *PSoC 4XX7_BLE Family Datasheet-Programmable System-on-Chip (PSoC)*. Accessed: Jan. 1, 2021. [Online]. Available: http://www.cypress.com/documentation/datasheets/psoc-4-psoc-4xx7ble-family-datasheet-programmable-system-chip-psoc

[9] S. Kamath and J. Lindh. (2012). AN092-measuring Bluetooth low energy power consumption. Texas Instruments. Accessed: Jan. 1, 2021. [Online]. Available: http://www.ti.com/product/CC2541

[10] G. Simon and M. Ratosi, "Characterization and measurement of performance properties of the UFSOOK camera communication protocol," *IEEE Trans. Instrum. Meas.*, vol. 69, no. 10, pp. 7982–7989, Oct. 2020.

[11] G. Simon, G. Zachár, and G. Vakulya, "Lookup: Robust and accurate indoor localization using visible light communication," *IEEE Trans. Instrum. Meas.*, vol. 66, no. 9, pp. 2337–2348, Sep. 2017.

[12] M. Z. Chowdhury, M. K. Hasan, M. Shahjalal, M. T. Hossan, and Y. M. Jang, "Optical wireless hybrid networks: Trends, opportunities, challenges, and research directions," *IEEE Commun. Surveys Tuts.*, vol. 22, no. 2, pp. 930–966, 2nd Quart. 2020.

[13] (Jun. 2021). *AM2302 Sensor*. Accessed: Jun. 8, 2021 [Online]. Available: https://datasheetspdf.com/pdf/942482/ETC/AM2302/1

[14] (Jun. 2021). *IEEE Standard for Local and Metropolitan Area Networks—Part 15.7: Short-Range Optical Wireless Communications Equivalent*. Accessed: Jun. 8, 2021. [Online]. Available: https://ieeexplore.ieee.org/stamp/stamp.jsp?tp=&arnumber=8697198

[15] M. Asim, F. Shamshad, and A. Ahmed, "Blind image deconvolution using deep generative priors," *IEEE Trans. Comput. Imag.*, vol. 6, pp. 1493–1506, 2020.

[16] V. H. Nguyen, M. D. Thieu, H. Nguyen, and Y. M. Jang, "Design and implementation of the MIMO–COOK scheme using an image sensor for long-range communication," *Sensors*, vol. 20, no. 8, p. 2258, Apr. 2020.

[17] T. Nguyen, M. D. Thieu, and Y. M. Jang, "2D-OFDM for optical camera communication: Principle and implementation," *IEEE Access*, vol. 7, pp. 29405–29424, 2019.

[18] M. F. Ahmed, M. K. Hasan, M. Shahjalal, M. M. Alam, and Y. M. Jang, "Experimental demonstration of continuous sensor data monitoring using neural network-based optical camera communications," *IEEE Photon. J.*, vol. 12, no. 5, pp. 1–11, Oct. 2020.

[19] T. S. Rajendra, Z. Stanislav, and G. Zabih, "Performance evaluation of neural network assisted motion detection schemes implemented within indoor optical camera based communications," *Opt. Exp.*, vol. 27, no. 17, pp. 24082–24092, 2019.

[20] S. Teli, W. A. Cahyadi, and Y. H. Chung, "Optical camera communication: Motion over camera," *IEEE Commun. Mag.*, vol. 55, no. 8, pp. 156–162, Aug. 2017.

[21] A. Sewaiwar, S. V. Tiwari, and Y. H. Chung, "Visible light communication based motion detection," *Opt. Exp.*, vol. 23, pp. 18769–18776, Jul. 2015.

[22] T. L. Pham, M. Shahjalal, V. Bui, and Y. M. Jang, "Deep learning for optical vehicular communication," *IEEE Access*, vol. 8, pp. 102691–102706, 2020.

[23] J. Lee, S. Kim, and S. Han, "Defocus based optical signal reception for distance enhanced optical camera communication," in *Proc. 21st Int. Conf. Transparent Opt. Netw. (ICTON)*, Angers, France, Jul. 2019, pp. 1–4.

[24] C. Lin *et al.*, "A blur equalization method for screen-to-camera based optical camera communications," in *Proc. 18th Int. Conf. Opt. Commun. Netw. (ICOCN)*, Huangshan, China, Aug. 2019, pp. 1–3.

[25] N. B. Hassan *et al.*, "Impact of camera lens aperture and the light source size on optical camera communications," in *Proc. 11th Int. Symp. Commun. Syst., Netw. Digit. Signal Process. (CSNDSP)*, Budapest, Hungary, Jul. 2018, pp. 1–5.

[26] *V81 Series Ball Valve*. Accessed: Jun. 8, 2021. [Online]. Available: https://www.dklokusa.com/wp-content/themes/dk/library/downloads/V81-7.pdf

[27] *ATtiny85*. Accessed: Jun. 8, 2021. [Online]. Available: https://www.microchip.com/wwwproducts/en/ATtiny85

[28] *C7837WIP IP Camera User Manual Shenzhen Vstarcam Technology*. Accessed: Jun. 8, 2021. [Online]. Available: https://fccid.io/2AOJ2-C7837WIP/User-Manual/User-Manual-3885406

[29] J.-W. Lee, S.-J. Kim, and S.-K. Han, "3D visible light indoor positioning by bokeh based optical intensity measurement in smartphone camera," *IEEE Access*, vol. 7, pp. 91399–91406 2019.

[30] J.-W. Lee, S.-J. Kim, and S.-K. Han, "Adaptive window thresholding for noise-robust photo detection in OCC," *Opt. Commun.*, vol. 426, pp. 623–628, Nov. 2018.

[31] Y. Ohira *et al.*, "Novel demodulation scheme based on blurred images for image-sensor-based visible light communication," in *Proc. IEEE Globecom Workshops (GC Wkshps)*, Dec. 2015, pp. 1–6.

[32] P. Huynh, T. H. Do, and M. A. Yoo, "Probability-based algorithm using image sensors to track the LED in a vehicle visible light communication system," *Sensors*, vol. 347, p. 17, Feb. 2017.

Md. Faisal Ahmed (Graduate Student Member, IEEE) received the B.Sc. degree in electrical and electronic engineering (EEE) from the Khulna University of Engineering & Technology (KUET), Khulna, Bangladesh, in 2019, and the M.Sc. degree in electronics engineering from Kookmin University, Seoul, South Korea, in August 2021, where he is currently pursuing the Ph.D. degree in electronics engineering with the Wireless Communication and Artificial Intelligence Laboratory.

His research interests include optical wireless communications (OWC), machine learning, deep learning, optical camera communication (OCC), convolutional neural networks (CNNs), wireless power transfer (WPT), and the IoT in a smart home, 5G, and 6G.

Moh Khalid Hasan (Graduate Student Member, IEEE) received the B.Sc. degree in electrical and electronic engineering (EEE) from the Khulna University of Engineering & Technology (KUET), Khulna, Bangladesh, in May 2017, and the M.Sc. degree in electronics engineering from Kookmin University, Seoul, South Korea, in August 2019. He is currently pursuing the Ph.D. degree in electrical and electronics engineering with the Stevens Institute of Technology, Hoboken, NJ, USA.

In September 2019, he joined the Wireless Communications and Artificial Intelligence Laboratory, Department of Electronics Engineering, Kookmin University, as a full-time Researcher. His current research interests include spectrum sharing, machine learning, and 6G.

Mr. Hasan received the Academic Excellence Award from Kookmin University for his research in 2019.

Mostafa Zaman Chowdhury (Senior Member, IEEE) received the B.Sc. degree in electrical and electronic engineering from the Khulna University of Engineering & Technology (KUET), Khulna, Bangladesh, in 2002, and the M.Sc. and Ph.D. degrees in electronics engineering from Kookmin University, Seoul, South Korea, in 2008 and 2012, respectively.

In 2003, he joined the Electrical and Electronic Engineering Department, KUET, as a Lecturer, where he is currently working as a Professor. He was a Post-Doctoral Researcher with Kookmin University from 2017 to 2019. He has published around 130 research papers in national and international conferences and journals. His research interests include convergence networks, QoS provisioning, small-cell networks, the Internet of Things, eHealth, 5G and beyond communications, and optical wireless communication.

Dr. Chowdhury has served as the TPC member for many IEEE conferences. He received the Excellent Student Award from Kookmin University in 2008. His three papers received the Best Paper Award at several international conferences around the world. He was involved in many Korean Government projects. He also received the Best Reviewer Award 2018 by *ICT Express* journal. Moreover, he also received the Education and Research Award 2018 given by Bangladesh Community in South Korea. He was the TPC Chair of the International Workshop on 5G/6G Mobile Communications in 2017 and 2018. He was/has been the Publicity Chair of the International Conference on Artificial Intelligence in Information and Communication 2019–2022. He has also served as a Reviewer for many international journals (including IEEE, Elsevier, Springer, ScienceDirect, MDPI, and Hindawi published journals) and IEEE conferences. He has been working as an Editor of *ICT Express*, an Associate Editor of IEEE ACCESS, an Associate Editor of *Frontiers in Communications and Networks*, a Lead Guest Editor of *Wireless Communications and Mobile Computing*, and a Guest Editor of *Applied Sciences*.

Nguyen Cong Hoan received the B.Sc. degree from the Automation Department, Ha Noi University of Science and Technology, Hanoi, Vietnam, in 2015, and the M.Sc. degree in electronics engineering from the Wireless Communication and Artificial Intelligence Laboratory, Kookmin University, Seoul, South Korea, in February 2021.

He worked with FPT Software, Hanoi, from 2015 to 2016, and Toshiba Software Development, Tokyo, Japan, from 2017 to 2018. His research interests include optical camera communication (OCC), Labview, and microcontroller programming.

Yeong Min Jang (Member, IEEE) received the B.E. and M.E. degrees in electronics engineering from Kyungpook National University, Daegu, South Korea, in 1985 and 1987, respectively, and the Ph.D. degree in computer science from the University of Massachusetts, Amherst, MA, USA, in 1999.

From 1987 to 2000, he was with the Electronics and Telecommunications Research Institute (ETRI), Gwangju, South Korea. Since 2002, he has been with the School of Electrical Engineering, Kookmin University, Seoul, South Korea, where was the Director of the Ubiquitous IT Convergence Center from 2005 to 2010. He has been the Director of the LED Convergence Research Center, Kookmin University, since 2010, the Director of the Internet of Energy Research Center, Kookmin University, since 2018, and the Director of the Telematics Research Institute, Kookmin University, since 2021. His research interests include 5G/6G mobile communications, the Internet of Energy, the IoT platform, AI platform, eHealth, smart factory, optical wireless communications, optical camera communication, AI mobility, and the Internet of Things.

Dr. Jang is also a fellow of the Korean Institute of Communications and Information Sciences (KICS). He had served as an Executive Director for KICS from 2006 to 2014. He was the President of KICS in 2019. He received the Young Scientist Award from the Korean Government from 2003 to 2006. He was a recipient of the Dr. Irwin Jacobs Award in 2018. He had also served as the Founding Chair for the KICS Technical Committee on Communication Networks in 2007 and 2008. He was/has been the Steering Chair of the Multi-Screen Service Forum from 2011 to 2019, and the Society Safety System Forum since 2015. He has also served as the Chairman for the IEEE 802.15 Optical Camera Communications Study Group in 2014, and the IEEE 802.15.7m Optical Wireless Communications Task Group from 2015 to 2019 and successfully published IEEE 802.15.7-2018 and ISO 22738:2020 standard. He has been the Chairman of IEEE 802.15.7a Higher Rate and Longer Range OCC TG, since 2020. He has organized several conferences and workshops, such as the International Conference on Ubiquitous and Future Networks from 2009 to 2017, the International Conference on ICT Convergence from 2010 to 2016, the International Workshop on Optical Wireless LED Communication Networks from 2013 to 2016, the International Conference on Information Networking in 2015, and the International Conference on Artificial Intelligence in Information and Communication since 2019. He is also the Editor-in-Chief of *ICT Express* (indexed by SCIE).